43

Mechanics of Debris Flows and Rock Avalanches

Richard M. Iverson
United States Geological Survey

43.1 Introduction

Debris flows are geophysical phenomena intermediate in character between rock avalanches and flash floods. They commonly originate as water-laden landslides on steep slopes and transform into liquefied masses of fragmented rock, muddy water, and entrained organic matter that disgorge from canyons onto valley floors. Typically including 50%–70% solid grains by volume, attaining speeds >10 m/s, and ranging in size up to ~10^9 m^3, debris flows can denude mountainsides, inundate floodplains, and devastate people and property (Figure 43.1). Notable recent debris-flow disasters resulted in more than 20,000 fatalities in Armero, Colombia, in 1985 and in Vargas state, Venezuela, in 1999.

Alternative terms such as mudflow, mudslide, debris torrent, and lahar are sometimes used to describe debris flows, but the terms "debris" and "flow" have precise geological meanings. "Debris" implies that grains with greatly differing sizes are present. The largest grains can exceed 10 m in diameter, but the presence of at least a few weight percent of mud-sized grains (<62 μm) is more critical because persistent hydrodynamic suspension of these small grains effectively increases the viscosity of the muddy water that fills pore spaces between the larger grains. This enhanced viscosity promotes development of high pore-fluid pressures that facilitate debris-flow motion by exerting lubrication forces at grain contacts. The term "flow" implies that slip at grain contacts is pervasive, and granular debris that is liquefied by high pore pressures can appear to flow almost as fluidly as water.

This chapter emphasizes the physical basis and mathematical structure of models that analyze two-phase debris-flow behavior by considering gravity-driven motion of granular solids that transport pore fluid with evolving pressure. In this modeling framework, granular rock avalanches represent a limiting class of flows in which effects of pore-fluid pressure are negligible. Differences between rock avalanches and debris flows can be gradational, however: relatively dry rock avalanches can sometimes engulf enough water to gradually transform to debris flows, for example. A further complication is that debris flows can occur in submarine environments, where water not only fills intergranular pores but also surrounds the flows and thereby exerts buoyancy and inertia forces. This chapter focuses exclusively on terrestrial flows in which the effects of the surrounding air are negligible.

43.2 Observations and Data

Although debris flows can be difficult and dangerous to observe directly, the chief qualitative features of debris-flow behavior can readily be observed in extensive video documentation obtained

Handbook of Environmental Fluid Dynamics, Volume One, edited by Harindra Joseph Shermal Fernando.

© 2013 CRC Press/Taylor & Francis Group, LLC.

ISBN: 978-1-4398-1669-1.

FIGURE 43.1 Oblique aerial photograph of a lethal debris flow that began as a rainfall-triggered landslide, Minamata, Japan, July 20, 2003. (After Sidle, R.C. and Chigira, M., *EOS*, 85, 145, 2004.) (Photo by courtesy of R.C. Sidle, Reproduced by permission of the American Geophysical Union.)

in the field and laboratory (e.g., Costa and Williams 1984; Logan and Iverson 2007):

1. Debris flows exhibit unsteady, nonuniform motion, with distinct starting and ending points in space and time. Debris-flow models must, therefore, include explicit time dependence.
2. Debris flows typically originate from discrete or distributed source areas that have slopes >30° mantled with soil and fragmented rock. This debris becomes thoroughly wet through introduction of surface water or groundwater, commonly as a result of intense rain or snowmelt. The water-laden debris starts to move downslope when frictional forces no longer can resist driving forces, and it then liquefies and begins to flow.
3. Many debris flows entrain additional sediment and water as they descend steep slopes and channels. Entrainment can occur by scour of bed material or collapse of stream banks, and it can cause the mass of a debris flow to increase 10-fold or more before deposition begins on flatter terrain downstream.
4. Abrupt, steep surge fronts generally form at the heads of moving debris flows. Large grains accumulate at surge fronts as a result of grain-size segregation and migration within the debris, but large grains can also be scoured from the bed and retained at surge fronts.
5. Water-saturated debris that trails surge fronts commonly resembles watery, flowing concrete or roiling quicksand. Thus, a debris-flow surge front commonly behaves as a "bouldery dam... pushed along by the finer, more fluid debris impounded behind..." (Sharp and Nobles 1953).
6. Lateral levees form where liquefied debris shoulders aside high-friction debris at surge fronts, most commonly where debris flows escape lateral confinement by overtopping stream banks or discharging onto broad alluvial fans or plains.
7. Depositional lobes form where the frictional resistance imposed by coarse-grained flow fronts and margins is sufficient to halt motion of the trailing, liquefied debris. Bodies of fresh debris-flow deposits are generally too weak for humans to traverse on foot, although the coarse-grained lateral levees and distal margins of fresh deposits commonly afford more secure footing.
8. Following emplacement, bodies of debris-flow deposits gradually dewater and consolidate to a degree that allows secure passage on foot. As desiccation proceeds, deposits become nearly rigid, but this process commonly requires several days to weeks.

Data that quantify many of the phenomena described above come from nearly field-scale experiments conducted in the 95 m long, 2 m wide USGS debris-flow flume (Iverson et al. 2010). A set of eight of these experiments in which the debris consisted of water-saturated sand and gravel containing 7% mud-sized grains (<62 μm) yielded results that contrast with those from a set of nine experiments that were identical in every respect, except that the mud content was <1%. In each of the 17 experiments, flow was initiated by suddenly releasing 10 m^3 of thoroughly mixed, loosely packed debris from behind a vertical headgate. The ensuing debris flows descended the 31° flume and swept past two instrumented cross sections (located at x = 32 and 66 m downslope from the headgate) before discharging onto a nearly flat runout surface and forming deposits at a third instrumented cross section (located at x = 90 m) (Figure 43.2). Each instrumented cross section was equipped with an overhead laser that measured the flow thickness and with bed sensors that measured basal normal stress and pore-fluid pressure at frequencies of 500 Hz.

Ensemble averages of the time-series data recorded at the instrumented cross sections provide comprehensive summaries of the behavior of the experimental debris flows. Each panel of Figure 43.3 depicts simultaneous evolution of the ensemble-averaged flow thickness, h, total basal normal stress, σ_{bed}, and basal pore-fluid pressure, p_{bed}, for a particular instrumented cross section and experiment set (identified as "SGM" for experiments with 7% mud content and as "SG" for experiments with <1% mud content). Vertical axes in Figure 43.3 are scaled so that the three time series in each panel exhibit perfect superposition if a liquefied state exists in which $p_{bed} = \sigma_{bed} = \rho g h$ (where $g \approx 9.8\,m/s^2$ is the magnitude of gravitational acceleration, and $\rho \approx 2040\,kg/m^3$ is a bulk density typical of water-saturated debris).

The most obvious implication of the data summarized in Figure 43.3 is that the fronts of SGM debris flows move downslope more rapidly than those of SG flows. The difference in

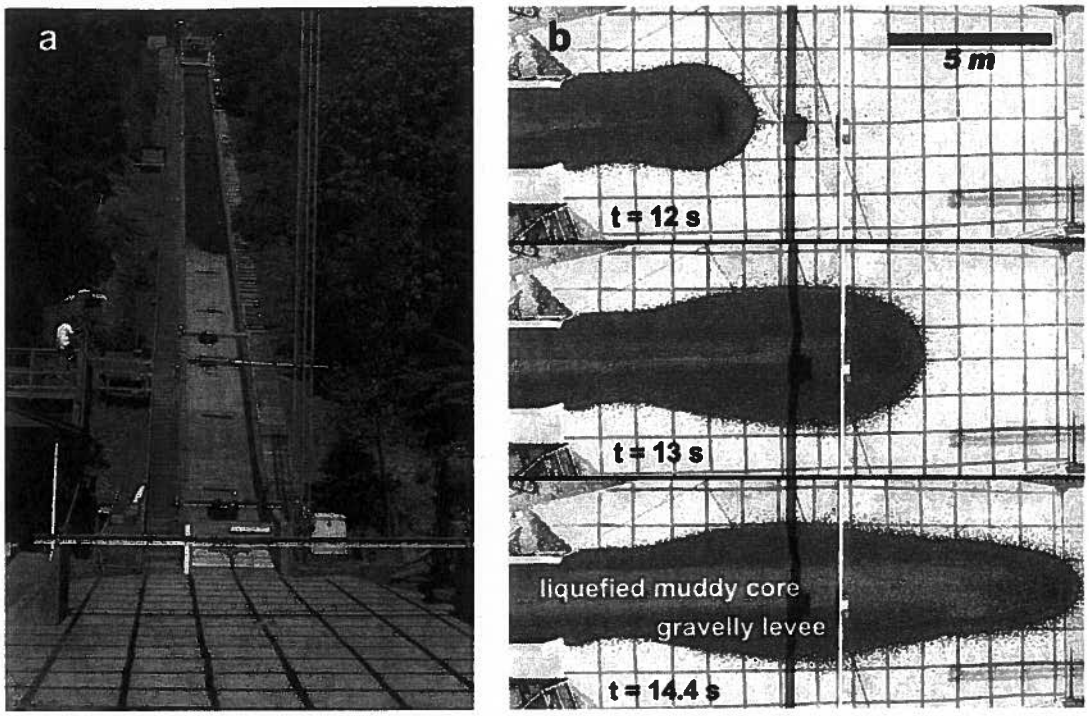

FIGURE 43.2 Photographs of a 10 m³ experimental debris flow in the USGS flume. (a) View of flow descending the flume. (b) Sequential aerial views of flow crossing runout surface and forming levees at base of flume. "t" denotes time elapsed since opening of headgate. Shadow is cast by crossbeam suspending laser at x = 90 m. (Reproduced from Iverson, R.M. et al., *J. Geophys. Res.*, 115, 2010, doi:10.1029/2009JF001514. With permission of the American Geophysical Union.)

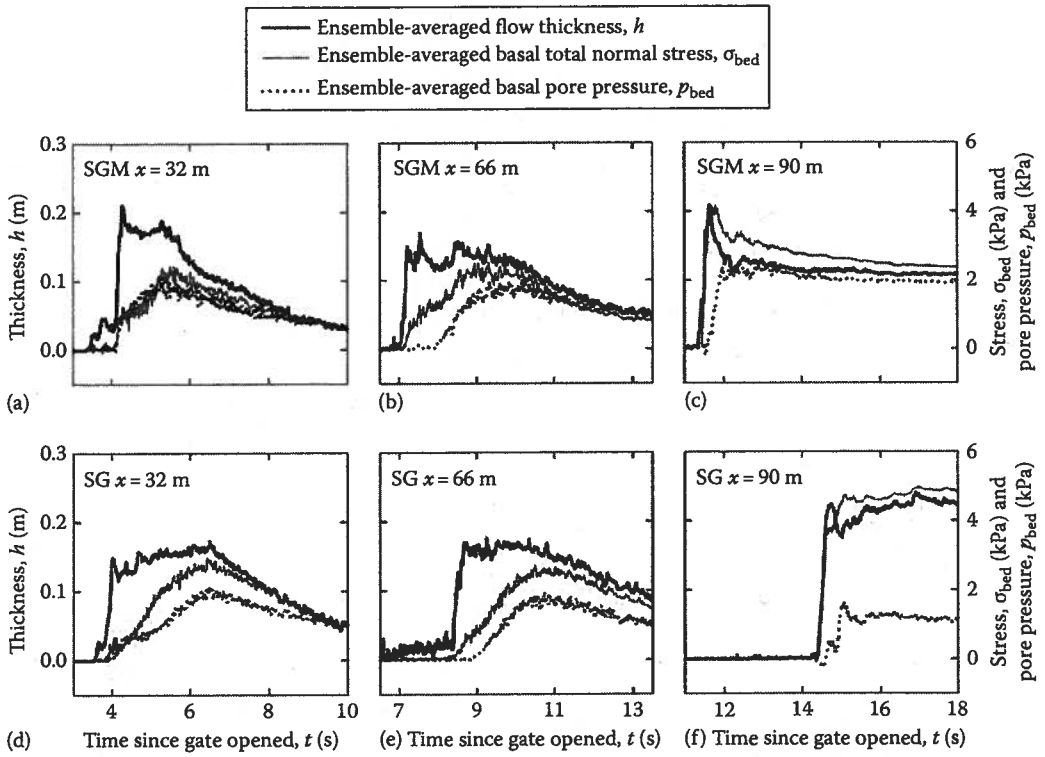

FIGURE 43.3 **(See color insert.)** Ensemble averages of flow thicknesses, basal total normal stresses, and basal pore-fluid pressures measured at three distances from the headgate (x = 32, 66, and 90 m) in two sets of experimental debris flows. (a–c) Data from eight SGM flows containing 7% mud. (d–f) Data from nine SG flows containing <1% mud. (Reproduced from Iverson, R.M. et al., *J. Geophys. Res.*, 115, 2010, doi:10.1029/2009JF001514. With permission of the American Geophysical Union.)

speeds takes time to develop; however, the fronts of both types of flows arrive at $x = 32$ m about $t = 4$ s after their release (cf. Figure 43.3a and d). This arrival time implies that all flows initially attain speeds only slightly less than that of a frictionless body, which theoretically reaches $x = 32$ m at $t = 3.56$ s when released on a 31° slope. The large initial flow-front speeds result not from near-zero friction, but instead from a strong downslope thrust (roughly proportional to $-\partial h/\partial x$) that is produced during collapse of the debris as the headgate opens. As this thrust diminishes, the effects of friction become more apparent: after $t = 4$ s, the SG flows begin to decelerate (arriving at $x = 66$ m at $t \approx 8.5$ s), but the SGM flows continue to accelerate (arriving at $x = 66$ m at $t \approx 7$ s). The disparity in SG and SGM arrival times grows to about 3 s when the flows reach $x = 90$ m (cf. Figure 43.3c and f). Furthermore, after the debris flows issue from the mouth of the flume, the SGM flows run out about twice as far as the SG flows (Iverson et al. 2010).

The high mobility of the SGM flows may seem counterintuitive, given that mud increases the viscosity of the fluid phase of the SGM, but relationships between the three time series in each of the upper panels of Figure 43.3 reveal the cause. The data in Figure 43.3a show that, after passage of a dilated, gravel-rich flow front from $t \approx 4$ to 6 s (wherein h averages roughly twice the magnitude of $\sigma_{bed}/\rho g$ and $p_{bed}/\rho g$), the approximation $p_{bed} = \sigma_{bed} = \rho g h$ holds reasonably well in SGM flows. This result implies that the debris trailing the dilated front at $x = 32$ m is almost completely liquefied by high pore-fluid pressure that reduces grain-contact stresses. Figure 43.3b and c show that this liquefaction persists at $x = 66$ and 90 m, although at these locations the rise in p_{bed} lags behind the rise in σ_{bed} because a more mature, coarse-grained flow front is present. Particularly noteworthy is the nearly perfect data superposition of time series in the final ~6 s shown in Figure 43.3c, which indicates that deposits behind the flow front are fully liquefied. Probing of the deposits demonstrates that the liquefied debris spreads into a thin puddle if it is not impounded by gravel-rich lateral levees like those pictured in Figure 43.2b.

Pore-pressure behavior in the SG flows differs markedly from that in the SGM flows. The differences first appear at $x = 32$ m, where p_{bed} remains significantly less than σ_{bed} during passage of most of the flow (Figure 43.3d). The discrepancy between p_{bed} and σ_{bed} grows more persistent at $x = 66$ m, and becomes most pronounced in deposits formed at $x = 90$ m (Figure 43.3e and f). Moreover, the SG deposits have $p_{bed} < 0.5\ \sigma_{bed}$, implying that the debris has not only lost some pore pressure but has also begun to dewater. Lack of sustained high pore pressure in the SG debris accounts for its relatively low mobility. Indeed, it may be appropriate to regard the behavior of the SG flows as intermediate between that of rock avalanches and true debris flows.

Irrespective of their differences, the SGM and SG flows both exhibit rapid formation and persistence of gravel-rich snouts, which are products of grain-size segregation. Videotapes of the experiments reveal that within the first 4 s of downslope travel, gravel migrates to the surface of the flows and then advances to the snouts, where much of it is retained (Logan and Iverson 2007). As the flows travel further downslope, the maturing gravelly snouts develop the pore-pressure deficits that are evident in Figure 43.3b through f. The pore-pressure deficits arise because of the high hydraulic permeability of the gravel, which makes it incapable of maintaining much pore pressure. As a result, gravelly snouts exert more frictional resistance than the liquefied, finer-grained debris that pushes them from behind.

43.3 Physical Principles Used in Modeling

The data summarized above illustrate the crucial role of evolving pore-fluid pressure in debris flows, and recent models have emphasized that debris consists of a distinct solid phase and fluid phase in which such pressure can exist (Iverson 1997; Iverson and Denlinger 2001; Savage and Iverson 2003; Pitman and Le 2005; Takahashi 2007; Kowalski 2008). The physical principles used to construct two-phase models of debris-flow dynamics involve concepts from continuum mixture theory, soil mechanics, and fluid mechanics, which are described below. Also described is the rationale for approximating two-phase debris flows as one-phase granular flows with evolving porosities and pore-fluid pressures.

43.3.1 Continuum Conservation Laws

For each phase of a debris-flow mixture individually, as well as for the mixture as a whole, the principle of mass conservation is expressed by

$$\frac{\partial \rho}{\partial t} + \nabla \cdot \rho \vec{v} = 0, \tag{43.1}$$

where

ρ is the mass density
$\vec{v}$ is the velocity vector
$\nabla \cdot \rho \vec{v}$ is the divergence of the linear momentum vector, $\rho \vec{v}$.

Conservation of linear momentum is expressed by

$$\frac{\partial \rho \vec{v}}{\partial t} + \nabla \cdot \rho \vec{v} \vec{v} = \rho \vec{g} - \nabla \cdot T, \tag{43.2}$$

where

$\vec{g}$ is the acceleration due to gravity
T is the stress (defined using a soil-mechanics convention in which compression is positive, because granular debris can sustain little or no tension)

Note that T and $\vec{v}\vec{v}$ are each 3 × 3 tensors, implying that $\nabla \cdot T$ and $\nabla \cdot \rho \vec{v}\vec{v}$ in (43.2) represent vectors rather than scalars obtained from vector divergences (e.g., Gidaspow 1994).

43.3.2 Density and Velocity Definitions

When mixture models are applied to debris flows, the solid and fluid constituents are generally assumed to have fixed mass densities, ρ_s and ρ_f, respectively. The definition of the mixture bulk density

$$\rho = \rho_s(1-n) + \rho_f n, \tag{43.3}$$

consequently shows that variation of the mixture porosity n wholly determines variation of ρ, provided that the debris remains fully saturated with pore fluid. Although n ranges from only about 0.3 in the densest debris flows to 0.5 in the most dilute, evolution of n plays a crucial role in debris-flow mechanics.

Like the mixture density, the mixture momentum is weighted by the mass of solid grains $\rho_s(1-n)$ and mass of pore fluid $\rho_f n$ per unit volume, but it also depends on the velocities of each phase. Thus, the linear momentum of the mixture is defined as $\rho\vec{v} = \vec{v}_s\rho_s(1-n) + \vec{v}_f\rho_f n$, where $\vec{v}_s$ is the velocity of the solid grains and $\vec{v}_f$ is the velocity of the pore fluid. This definition of mixture momentum implies that the mixture velocity is defined as

$$\vec{v} = \frac{\vec{v}_s\rho_s(1-n) + \vec{v}_f\rho_f n}{\rho}. \tag{43.4}$$

If separate momentum-conservation equations are written for the solid and fluid phases, these equations sum to yield the momentum-conservation equation for the mixture as a whole only if the mixture velocity is defined as in (43.4).

Another velocity that plays a key role in debris-flow mechanics is the pore-fluid velocity relative to the solid velocity, $\vec{v}_f - \vec{v}_s$. To an observer moving with the local solid velocity $\vec{v}_s$, the apparent fluid velocity is the volumetric flux of pore fluid per unit area of mixture, $\vec{q}$:

$$\vec{q} = n(\vec{v}_f - \vec{v}_s). \tag{43.5}$$

In porous media theory, $\vec{q}$ is known as the specific discharge (Bear 1972).

The definition of $\vec{q}$ can be combined algebraically with Equations 43.3 and 43.4 to obtain the important relationship

$$\frac{\vec{v}}{\vec{v}_s} = \frac{\rho_f}{\rho}\frac{\vec{q}}{\vec{v}_s} + 1. \tag{43.6}$$

For debris flows this relationship commonly reduces to $\vec{v}/\vec{v}_s \approx 1$, because values $\rho_f/\rho \approx 1/2$, $\vec{v}_s > 0.1$ m/s, and $\vec{q} \ll 0.1$ m/s are typical. The approximation $\vec{v}/\vec{v}_s \approx 1$ allows the mixture momentum to be approximated as $\rho\vec{v}_s$, thereby reducing the two-phase flow problem to an equivalent one-phase problem in which $\vec{v}_s$ (or $\vec{v}$) is influenced by the solid–fluid interaction stress associated with $\vec{q}$.

43.3.3 Effective Stress and Pore-Fluid Pressure

The use of an equivalent one-phase formulation implies that the stress T in (43.2) must account for all solid–fluid interaction stresses, including those due to $\vec{q}$ (Iverson 1997). A simple but nevertheless useful approach to this problem employs a key concept from soil mechanics: the effective stress principle. This principle states that the total stress tensor T can be decomposed into components of stress borne by the solid and fluid phases, such that

$$T = T_e + Ip + nT_{vis}, \tag{43.7}$$

where

- T_e is the effective stress borne by the solid grains
- p is the pressure borne by the fluid
- I is the identity tensor
- T_{vis} is the deviatoric fluid stress that results from macroscopic viscous shearing

The stresses T_e and p are treated as if they act throughout the entire mixture, whereas T_{vis} acts only within the fluid volume fraction n. Separation of the fluid stresses in (43.7) into an isotropic component p and deviatoric component T_{vis} is similar to the convention used in fluid mechanics, but it differs owing to the definition of p as a mixture-spanning quantity.

The most important ramification of (43.7) is that increases in the pore-fluid pressure p imply attendant reductions in the mean effective normal stress borne by the solid grains, σ_e (where σ_e is a scalar equaling the mean of the diagonal components of the tensor T_e). This normal-stress reduction reduces intergranular Coulomb friction and thereby facilitates debris-flow motion.

43.3.4 Coulomb Friction

Coulomb friction generates most of the shear stress in debris flows and in other dense granular flows (Iverson 1997). In its simplest form the Coulomb friction rule states that the maximum shear resistance attainable before intergranular slip occurs is equal to the product of a constant friction coefficient and the normal stress at grain contacts. Furthermore, as slip occurs, the shear stress retains this limiting equilibrium value.

Two important modifications of the Coulomb friction rule pertain to debris flows. The first involves application of the effective-stress principle (43.7), which states that T_e is the relevant normal stress at grain contacts. The second modification accounts for the observation that the intergranular friction coefficient $\tan\phi$ can evolve as the shear rate and effective normal stress evolve. (This chapter expresses friction coefficients by using the tangent of the friction angle, ϕ, which is similar to the steepest angle of repose attainable by a static, tabular layer of grains.) These modifications result in a Coulomb friction rule expressed in 1D form as

$$\tau_s = -\mathrm{sgn}(\vec{v})[\sigma_s - p_s]\tan\phi(S), \tag{43.8}$$

where

- τ_s is the shear stress on a plane of slippage
- $-\mathrm{sgn}(\vec{v})$ denotes that this shear stress always resists motion
- σ_s and p_s are the total normal stress and pore-fluid pressure acting on the same plane as τ_s
- $\phi(S)$ denotes dependence of ϕ on the state parameter S

Multidimensional versions of (43.8) can be formulated, but they require considerable tensor algebra, a topic best reserved for detailed treatises (e.g., Desai and Siriwardane 1984).

The importance of the dimensionless parameter S in (43.8) has recently been emphasized by Forterre and Pouliquen (2008), among others; and for application to debris flows, S can be defined as

$$S = \frac{\rho_s \dot{\gamma}^2 \delta^2}{\sigma_e}, \tag{43.9}$$

where

- $\dot{\gamma}$ is the local shear rate (which has dimensions of t^{-1})
- δ is the characteristic diameter of grains involved in the shearing
- σ_e is the mean effective normal stress defined above (Iverson et al. 2010)

Physically, S expresses the ratio of grain-scale inertial stresses (caused by dynamic grain interactions during shearing) to bulk-scale quasi-static stresses (caused by gravitational forces and reduced by pore-fluid pressure). Experiments and simulations indicate that $\tan\phi$ increases smoothly as a function of S, although variation of $\tan\phi$ is probably less than twofold over the entire domain $S = 0$ to $S \to \infty$. Remarkably, even in the limit $S \to \infty$, which indicates a liquefied state in which granular momentum exchange occurs by brief collisions rather than enduring friction at grain contacts, τ_s obeys an equation analogous to (43.8), as first demonstrated long ago by Bagnold (Hunt et al. 2002).

The Coulomb friction rule (43.8) applies to flow boundaries as well as flow interiors. Values of $\tan\phi$ along boundaries can differ from those in interiors, however, and these differences can be crucial because boundary slip can be responsible for a large fraction of the total frictional energy dissipation in debris flows (Iverson et al. 2010).

43.3.5 Dilatancy and Porosity Change

Granular materials like those in debris flows can exhibit porosity change for several reasons. Mathematically, the rate of porosity change is related to the dilation rate (i.e., the divergence of the solid grain velocity, $\nabla \cdot \vec{v}_s$) by

$$\nabla \cdot \vec{v}_s = \frac{1}{1-n}\frac{dn}{dt}, \tag{43.10}$$

where $d/dt = \partial/\partial t + \vec{v}_s \cdot \nabla$ is a total time derivative in a frame of reference that moves with the granular velocity $\vec{v}_s$ (Bear 1972). If porosity change occurs in response to shearing, the phenomenon is known as dilatancy. In densely packed states, rotund grains must move apart (exhibiting positive dilatancy) to attain sufficient space to shear past one another, whereas in loosely packed states they contract (exhibiting negative dilatancy) as shearing occurs.

In debris flows the net dilation rate depends on two interacting effects: dilatancy associated with shearing and compression caused by increases in the mean effective normal stress, σ_e. Iverson (2009) proposed that the net dilation rate can be expressed by a linear sum of these effects, yielding

$$\nabla \cdot \vec{v}_s = \dot{\gamma}\psi - \alpha\frac{d\sigma_e}{dt}, \tag{43.11}$$

where ψ is the debris' shear-induced dilatancy (a dimensionless quantity commonly expressed as an angle, $-\pi/2 \le \psi \le \pi/2$), and α is the debris' compressibility (the reciprocal of a bulk modulus). Note that if shearing of debris were to occur in a closed container that imposes the condition $\nabla \cdot \vec{v}_s = 0$, then (43.11) reduces to $d\sigma_e/dt = \dot{\gamma}\psi/\alpha$, which implies that σ_e increases with time if shearing proceeds at a constant rate $\dot{\gamma}$ with constant $\psi > 0$. This specious prediction demonstrates that ψ cannot be a material constant. Rather, it must evolve and ultimately become zero during steady-state shearing with no volume change. In soil mechanics this type of steady state is known as a critical state.

Experiments show that the dilatancy ψ evolves in a manner that depends on the current value of n relative to a value n_{eq} that is in equilibrium with the ambient state of stress and shear rate, and that this dependence roughly obeys a linear relation, $\psi = -C_1(n - n_{eq})$, where C_1 is a positive constant of order 1 (Pailha and Pouliquen 2009). Other experiments demonstrate that the dependence of n_{eq} on the ambient state of stress and shear rate can be summarized as a dependence on S (Forterre and Pouliquen 2008). Although the exact form of this dependence has not been determined for debris-flow materials, the relation $\psi = -C_1[n - n_{eq}(S)]$ can nevertheless be combined with (43.10) and (43.11) to infer that a differential equation describing evolution of n is (cf. Iverson 2009; Pailha and Pouliquen 2009)

$$\frac{dn}{dt} = C_1\dot{\gamma}(n-1)[n - n_{eq}(S)] - \alpha(1-n)\frac{d\sigma_e}{dt}. \tag{43.12}$$

The implications of (43.12) can be complicated, but some insight can be gained by assuming that $d\sigma_e/dt = 0$ and that $\dot{\gamma}$ and S are constants, such that n_{eq} is also a constant and evolution of n is decoupled from evolving debris-flow dynamics. Then an exact solution of (43.12) demonstrates that n relaxes exponentially toward its equilibrium value, n_{eq}, with a relaxation time $1/(1 - n_{eq})C_1\dot{\gamma}$. This result implies that the speed of porosity relaxation is directly proportional to the shear rate $\dot{\gamma}$—but only if changes in σ_e and S do not intercede.

43.3.6 Excess Pore-Fluid Pressure and Darcy Drag

Equation 43.12 indicates that porosity evolution depends not only on shear-induced dilatancy but also on evolution of the mean effective normal stress, σ_e (and, thus, on evolution of

pore-fluid pressure). Indeed, evolution of porosity implies that relative motion of the solid and fluid phases must occur (i.e., $\vec{v}_f - \vec{v}_s \neq 0$), and this relative motion necessarily results in momentum exchange that modifies pore-fluid pressure. In debris-flow mechanics it is conventional to approximate the effects of solid–fluid momentum exchange by using a simple linear drag rule (Darcy's law), which can be expressed as

$$\vec{q} = n(\vec{v}_f - \vec{v}_s) = -\frac{k}{\mu}\nabla p_e, \tag{43.13}$$

where

$\vec{q}$ is the specific discharge defined in (43.5)
k is the hydraulic permeability of the granular assemblage (a quantity with dimensions of length squared)
μ is the viscosity of the pore fluid

The quantity p_e is the "excess" pore-fluid pressure defined as $p_e = p - \rho_f g(h - z)\cos\theta$, where p is the total pore-fluid pressure, and $\rho_f g(h - z)\cos\theta$ is the hydrostatic equilibrium pressure at a slope-normal height z in a debris flow of thickness h on a slope with angle θ. Values of k for typical debris-flow materials range from about 10^{-13} to 10^{-8} m^2, and values of μ for muddy pore fluid range from about 10^{-2} to 10 Pa-s, so that k/μ ranges from about 10^{-14} to 10^{-6} m^2/Pa s. As a consequence, (43.13) implies that very significant excess pore-pressure gradients ($\nabla p_e \sim \rho_f g \sim 10^4$ Pa/m) will develop in reaction to solid–fluid momentum exchange if the magnitude of $\vec{q}$ exceeds 10^{-2} m/s for debris flows with the largest k/μ values and if it exceeds 10^{-10} m/s for debris flows with the smallest k/μ values. The large excess pore-pressure gradients associated with these $\vec{q}$ magnitudes tend to inhibit development of greater $\vec{q}$ magnitudes, owing to the effects of pore-pressure diffusion.

43.3.7 Pore-Pressure Diffusion

The relationship between the porosity change described by (43.10) and the excess pore-pressure gradient described by (43.13) implies that pore-pressure evolution is mathematically analogous to forced diffusion. This analogy is revealed by first observing that, if the mixture remains saturated, mass conservation dictates that the divergence of the solid grain velocity $\nabla \cdot \vec{v}_s$ in (43.10) must be balanced by a counter-flow of pore fluid, such that

$$\nabla \cdot \vec{v}_s = -\nabla \cdot \vec{q}. \tag{43.14}$$

Substitution of (43.13) and (43.14) into (43.10) then yields a fundamental equation that shows how porosity change is related to the divergence of ∇p_e:

$$\frac{1}{1-n}\frac{dn}{dt} = \nabla \cdot \frac{k}{\mu}\nabla p_e. \tag{43.15}$$

The porosity n can be eliminated from this equation by combining (43.15) with (43.10) and (43.11) to obtain an equation with $d\sigma_e/dt$ on the left-hand side. For the case in which k/μ is constant, this equation reduces to

$$\frac{d\sigma_e}{dt} = -\frac{k}{\alpha\mu}\nabla^2 p_e + \frac{\dot{\gamma}\psi}{\alpha}, \tag{43.16}$$

where $k/\alpha\mu$ plays the role of a pore-pressure diffusivity (which has dimensions of length squared per unit time). Finally, the definition of effective stress (43.7) can be used to infer that $d\sigma_e/dt = d\sigma/dt - dp_e/dt - d[\rho_f g(h - z)\cos\theta]/dt$, where σ is the mean total stress, and substitution of this relationship in (43.16) enables the equation to be recast as a forced, advection-diffusion equation for p_e,

$$\frac{dp_e}{dt} - \frac{k}{\alpha\mu}\nabla^2 p_e = \frac{d}{dt}[\sigma - \rho_f g(h-z)\cos\theta] - \frac{\dot{\gamma}\psi}{\alpha}. \tag{43.17}$$

The total time derivative $dp_e/dt = \partial p_e/\partial t + \vec{v}_s \cdot \nabla p_e$ on the left-hand side of (43.17) includes the effects of advection, and the forcing terms on the right-hand side of (43.17) express the evolving effects of the shear-induced dilation rate $\dot{\gamma}\psi$, the mean total stress σ, and the hydrostatic pore-pressure component $\rho_f g(h - z)\cos\theta$. Note that if all of the time derivatives in (43.17) are zero and $\dot{\gamma}\psi$ is constant, the equation reduces to the steady-state balance $(k/\mu)\nabla^2 p_e = \dot{\gamma}\psi$, which can alternatively be written as $-\nabla \cdot \vec{q} = \dot{\gamma}\psi$. This result shows that porosity creation during steady dilation is balanced by a steady influx of fluid that fills the enlarging pores.

The forcing effects described by the right-hand side of (43.17) can drive pore-pressure change, but p_e can evolve even in the absence of forcing owing to diffusion described by the left-hand side of (43.17). Normalization of the left-hand side of (43.17) shows that excess pore pressure relaxes diffusively with a characteristic time $h^2\alpha\mu/k$. This relaxation time includes not only the pore-pressure diffusivity $k/\alpha\mu$ but also the square of the debris-flow thickness h, which is the length scale over which pore-pressure diffusion typically occurs. Owing to this dependence on h^2, pore-pressure relaxation proceeds more slowly in large debris flows than in small ones. Thus, once excess pore pressure develops, large debris flows can maintain lower Coulomb friction and exhibit greater mobility than can small flows.

43.3.8 Disparate Relaxation Times and Limits on Feedback

Equations 43.12, 43.15, and 43.17 indicate a strong interdependence between evolution of porosity, dilatancy, excess pore-fluid pressure, and effective stress. They also show that a large disparity exists between the characteristic timescales for porosity relaxation in the absence of pore pressure ($1/(1 - n_{eq})C_1\dot{\gamma}$ commonly ~ 1 s) and for dissipation of excess pore-fluid pressure that occurs in response to porosity change ($h^2\alpha\mu/k$ commonly $> 10^3$ s). Such disparate values imply that the inherently fast process of

shear-induced porosity change can rapidly generate pore-pressure changes that inhibit further porosity change. Thus, in the absence of changes in forcing (such as changes in bed slope that drive changes in $\dot{\gamma}$), diffusive pore-pressure responses tend to stabilize debris-flow motion by regulating pore-pressure feedback that influences frictional resistance to flow.

Pore-pressure feedback may also be subject to lower and upper bounds due to phenomena not explicitly represented in (43.12), (43.15), and (43.17). For example, the effective lower limit on pore-fluid pressure in debris flows is probably zero (i.e., the atmospheric reference pressure). Negative pore pressures might occur in dewatering debris, but they would result from surface tension at air–water interfaces (i.e., meniscuses) in partly filled pore spaces, and such delicate features seem unlikely to have significant effects on agitated, coarse-grained debris. To date, debris-flow models have ignored them. A practical upper bound on pore-fluid pressure in debris flows is probably the liquefaction pressure, $p = \sigma$, which produces $\sigma_e = 0$. Higher pore pressures theoretically could be produced by forced debris contraction, but the propensity for contraction largely vanishes as $\sigma_e \to 0$.

43.3.9 Effects of Grain-Size Segregation

The development and dissipation of excess pore-fluid pressure described by (43.17) underscores the significance of grain-size segregation in debris flows, because the value of k in (43.17) depends strongly on the local grain grain-size distribution. As discussed in Section 43.2, grain-size segregation leads to a characteristic debris-flow architecture in which coarse-grained, high-friction snouts that lack much pore pressure impede the motion of trailing, liquefied, fine-grained debris. At present no satisfactory model exists for predicting grain-size segregation in debris flows, although recent advances in granular mechanics indicate that progress may be forthcoming (Gray and Kokelaar 2010). A stopgap approach mimics the effect of grain-size segregation by specifying a heterogeneous k distribution (Savage and Iverson 2003).

43.3.10 Boundary Erosion and Mass Change

As noted in Section 43.2, debris flows commonly gain mass as they descend steep, erodible slopes and channels, and they begin to lose mass and form deposits when they reach flatter terrain. No precise criteria exist for determining where this transition occurs, however, and no widely accepted formula exists for predicting the rate of mass change. Many debris-flow models, such as the one described in the following, account for the *effects* of mass change in conservation laws, but they take no account of the forces necessary to *cause* the mass change. Better understanding of the mechanics of mass change awaits further research.

43.4 Model Formulation and Analysis

Key steps in the development of most mathematical models of debris-flow motion include depth integration of the governing equations and shallow-flow scaling that justifies neglect of some terms. Depth integration removes the explicit appearance of one velocity component (here denoted by v_y) and thereby reduces the number of dependent variables. It also embeds, within the conservation equations, kinematic boundary conditions that describe the position of the free upper surface and basal flow boundary, thereby eliminating the need to track motion of these boundaries separately. Finally, it readily incorporates mass-change terms that describe fluxes of debris through the upper and basal boundaries.

Because of the need to specify the direction of depth integration (the z direction) *a priori*, the choice of a coordinate system is crucial. Some models use an Earth-centered, orthogonal Cartesian coordinate system with z vertical, which has the advantage of being universal and independent of terrain geometry. Such a system leads to complicated mechanical considerations when computing motion across steep, irregular slopes, however (Denlinger and Iverson 2004). Other models, including the one presented here, use a z coordinate normal to the local ground surface, such that the x coordinate is directed downslope and the y coordinate cross-slope (Figure 43.4). This approach simplifies the mechanics, but it requires use of curvilinear coordinate systems to adapt it to natural terrain. This chapter omits consideration of the complex mathematics associated with curvilinear coordinates, and instead focuses on the mechanical implications of depth-integrated conservation laws.

43.4.1 Depth-Integrated Conservation Laws with Mass and Bulk-Density Change

Consider motion of a debris flow of variable bulk density ρ moving down a planar slope inclined at the angle θ (Figure 43.4). (Recall from (43.3) that a simple relation exists between variations in debris-flow bulk density and porosity, provided that the

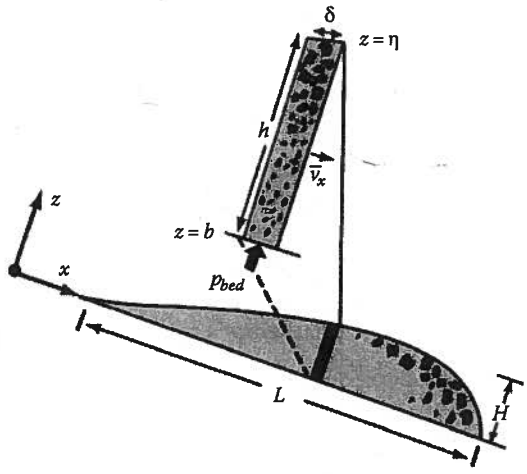

FIGURE 43.4 Schematic vertical cross section of a debris flow descending a uniform slope inclined at the angle θ. The x–z coordinate system and flow length scales H and L are defined. Magnified slice illustrates the dependent variables, $\bar{v}_x$, h, and p_{bed} as well as a local grain length scale, δ. (Reproduced from Iverson, R.M. et al., *J. Geophys. Res.*, 115, 2010, doi:10.1029/2009JF001514. With permission of the American Geophysical Union.)

flow remains saturated with pore fluid. Thus, a variable-bulk-density model can be used in place of a variable-porosity model, and it can be extended to include cases with variable saturation.) The vector conservation laws (43.1) and (43.2) imply that the scalar equations describing conservation of mass and the downslope (x) component of linear momentum are

$$\frac{\partial \rho}{\partial t}+\frac{\partial(\rho v_x)}{\partial x}+\frac{\partial(\rho v_y)}{\partial y}+\frac{\partial(\rho v_z)}{\partial z}=0, \tag{43.18}$$

$$\frac{\partial(\rho v_x)}{\partial t}+\frac{\partial(\rho v_x^2)}{\partial x}+\frac{\partial(\rho v_x v_y)}{\partial y}+\frac{\partial(\rho v_x v_z)}{\partial z}$$
$$=\rho g_x-\frac{\partial \tau_{xx}}{\partial x}-\frac{\partial \tau_{yx}}{\partial y}-\frac{\partial \tau_{zx}}{\partial z}=\Sigma F_x, \tag{43.19}$$

where v_x, v_y and v_z, are, respectively, the x, y, and z components of the debris velocity (either $\vec{v}$ or $\vec{v}_s$, as described in Section 43.3); $\rho g_x = \rho g \sin\theta$ is the x component of the debris weight per unit volume; τ_{xx}, τ_{yx} and τ_{zx} are the components of the stress tensor acting in the x direction; and ΣF_x is shorthand notation for the sum of the weight and stress terms. Equations analogous to (43.19) describe conservation of the y and z momentum components.

Depth averages of the dependent variables in (43.18) and (43.19) are defined as

$$\bar{\rho}(x,y,t)=\frac{1}{h}\int_b^\eta \rho dz \quad \bar{v}_x(x,y,t)=\frac{1}{h}\int_b^\eta v_x dz$$
$$\bar{v}_y(x,y,t)=\frac{1}{h}\int_b^\eta v_y dz \quad \bar{v}_z(x,y,t)=\frac{1}{h}\int_b^\eta v_z dz, \tag{43.20}$$

where $z = b(x, y, t)$ is the position of the debris-flow base, $z = \eta(x, y, t)$ is the position of the free upper surface, and $h(x, y, t) = \eta - b$ is the flow thickness (Figure 43.4). Subsequent equations are simplified by assuming that ρ varies only as a function of x, y, and t, such that $\rho = \bar{\rho}$. Similar assumptions are necessary in any depth-integrated model.

Integration of (43.18) and (43.19) through the debris-flow thickness from its base at $z = b$ to its upper surface at $z = \eta$ employs kinematic boundary conditions that relate $v_z(b)$ and $v_z(\eta)$ to the other velocity components at $z = b$ and $z = \eta$ and to variations in the boundary positions:

$$v_z(b)=\frac{\partial b}{\partial t}+v_x(b)\frac{\partial b}{\partial x}+v_y(b)\frac{\partial b}{\partial y}-B(x,y,t), \tag{43.21}$$

$$v_z(\eta)=\frac{\partial \eta}{\partial t}+v_x(\eta)\frac{\partial \eta}{\partial x}+v_y(\eta)\frac{\partial \eta}{\partial y}-A(x,y,t). \tag{43.22}$$

Here A and B are the boundary-migration velocities (positive upward) caused by the possible entry of debris at the free upper surface or basal surface of the flow, respectively. For example, if a static heap of debris with $v_x = v_y = v_z = 0$ is subject to upper-surface accretion at a rate $A > 0$, (43.22) shows that the heap's height η increases at the rate $\partial\eta/\partial t = A$. The situation is more complicated at the base of a moving debris flow, where either erosion or sedimentation can occur and all of the terms in (43.21) can evolve simultaneously, but $B > 0$ always characterizes upward bed migration due to sedimentation, and $B < 0$ characterizes bed lowering due to erosion. Subsequent equations assume that the bulk density of bed and bank material potentially incorporated in the debris flow locally equals $\bar{\rho}$ of the flow itself.

For the case with $\rho = \bar{\rho}$, depth integration of the mass-conservation Equation 43.18 yields

$$\int_b^\eta\left[\frac{\partial \bar{\rho}}{\partial t}+\frac{\partial(\bar{\rho}v_x)}{\partial x}+\frac{\partial(\bar{\rho}v_y)}{\partial y}+\frac{\partial(\bar{\rho}v_z)}{\partial z}\right]dz$$
$$=h\frac{\partial \bar{\rho}}{\partial t}+h\bar{v}_x\frac{\partial \bar{\rho}}{\partial x}+h\bar{v}_y\frac{\partial \bar{\rho}}{\partial y}+\bar{\rho}\left[v_z(\eta)-v_z(b)\right]$$
$$+\bar{\rho}\left[\frac{\partial}{\partial x}\int_b^\eta v_x dz-v_x(\eta)\frac{\partial \eta}{\partial x}+v_x(b)\frac{\partial b}{\partial x}\right.$$
$$\left.+\frac{\partial}{\partial y}\int_b^\eta v_y dz-v_y(\eta)\frac{\partial \eta}{\partial y}+v_y(b)\frac{\partial b}{\partial y}\right]$$
$$=h\frac{\partial \bar{\rho}}{\partial t}+\frac{\partial(\bar{\rho}h\bar{v}_x)}{\partial x}+\frac{\partial(\bar{\rho}h\bar{v}_y)}{\partial y}-\bar{\rho}\left[v_x(\eta)\frac{\partial \eta}{\partial x}+v_y(\eta)\frac{\partial \eta}{\partial y}-v_z(\eta)\right]$$
$$+\bar{\rho}\left[v_x(b)\frac{\partial b}{\partial x}+v_y(b)\frac{\partial b}{\partial y}-v_z(b)\right]$$
$$=\frac{\partial(\bar{\rho}h)}{\partial t}+\frac{\partial(\bar{\rho}h\bar{v}_x)}{\partial x}+\frac{\partial(\bar{\rho}h\bar{v}_y)}{\partial y}-\bar{\rho}A+\bar{\rho}B=0. \tag{43.23}$$

The third and fourth lines of (43.23) illustrate the result of using Leibniz rule for interchanging the order of integration and differentiation during evaluation of $\int_b^\eta[\partial v_x/\partial x]dz$ and $\int_b^\eta[\partial v_y/\partial y]dz$. The last line of (43.23) results from substituting the kinematic boundary conditions (43.21) and (43.22) into the fifth and sixth lines of (43.23) in place of $v_z(\eta)$ and $v_z(b)$, and then cancelling terms that sum to zero and making the identification $\partial(\eta - b)/\partial t = \partial h/\partial t$. If $A = B = 0$ and $\bar{\rho}$ is constant, then Equation 43.23 reduces to the form of the mass-conservation equation used in standard shallow-water flow theory, $\partial h/\partial t + \partial(h\bar{v}_x)/\partial x + \partial(h\bar{v}_y)/\partial y = 0$.

Depth integration of the x-component momentum-conservation Equation (43.19) employs Leibniz rule and uses

the kinematic boundary conditions (43.21) and (43.22) to cancel many terms. For the case with $\rho = \bar{\rho}$ the integration yields

$$\begin{aligned}
&\int_b^\eta \left[\frac{\partial(\bar{\rho}v_x)}{\partial t} + \frac{\partial(\bar{\rho}v_x^2)}{\partial x} + \frac{\partial(\bar{\rho}v_xv_y)}{\partial y} + \frac{\partial(\bar{\rho}v_xv_z)}{\partial z} \right] dz \\
&= \frac{\partial}{\partial t}\bar{\rho}\int_b^\eta v_x dz - \bar{\rho}v_x(\eta)\frac{\partial \eta}{\partial t} + \bar{\rho}v_x(b)\frac{\partial b}{\partial t} \\
&+ \frac{\partial}{\partial x}\bar{\rho}\int_b^\eta v_x^2 dz - \bar{\rho}v_x^2(\eta)\frac{\partial \eta}{\partial x} + \bar{\rho}v_x^2(b)\frac{\partial b}{\partial x} \\
&+ \frac{\partial}{\partial y}\bar{\rho}\int_b^\eta v_xv_y dz - \bar{\rho}v_x(\eta)v_y(\eta)\frac{\partial \eta}{\partial y} + \bar{\rho}v_x(b)v_y(b)\frac{\partial b}{\partial y} \\
&+ \bar{\rho}v_x(\eta)v_z(\eta) - \bar{\rho}v_x(b)v_z(b) \\
&= \frac{\partial(\bar{\rho}h\bar{v}_x)}{\partial t} + \frac{\partial(\bar{\rho}h\bar{v}_x^2)}{\partial x} + \frac{\partial(\bar{\rho}h\bar{v}_x\bar{v}_y)}{\partial y} \\
&+ \frac{\partial}{\partial x}\bar{\rho}\int_b^\eta (v_x - \bar{v}_x)^2 dz + \frac{\partial}{\partial y}\bar{\rho}\int_b^\eta (v_x - \bar{v}_x)(v_y - \bar{v}_y) dz - \bar{\rho}v_x(\eta)A \\
&+ \bar{\rho}v_x(b)B \\
&= \int_b^\eta \Sigma F_x dz. \qquad (43.24)
\end{aligned}$$

The integrals in the seventh line of (43.24) arise from the use of the identities

$$\begin{aligned}
\int_b^\eta v_x^2\, dz &= h\bar{v}_x^2 + \int_b^\eta (v_x - \bar{v}_x)^2 dz \\
\int_b^\eta v_xv_y dz &= h\bar{v}_x\bar{v}_y + \int_b^\eta (v_x - \bar{v}_x)(v_y - \bar{v}_y) dz, \qquad (43.25)
\end{aligned}$$

which show how the depth integrals of products are related to the products of depth integrals. Physically, the integrands $(v_x - \bar{v}_x)^2$ and $(v_x - \bar{v}_x)(v_y - \bar{v}_y)$ in (43.24) and (43.25) describe the effects of differential advection of momentum due to variations of v_x and v_y with depth z. Most debris-flow models neglect these effects and assume that $v_x = \bar{v}_x$ and $v_y = \bar{v}_y$, and the same approach is used here. Differential advection of momentum might play a particularly important role, however, if erosion or deposition occurs and velocity gradients near the bed are significant.

With neglect of the differential advection terms, (43.24) reduces to

$$\frac{\partial(\bar{\rho}h\bar{v}_x)}{\partial t} + \frac{\partial(\bar{\rho}h\bar{v}_x^2)}{\partial x} + \frac{\partial(\bar{\rho}h\bar{v}_x\bar{v}_y)}{\partial y} = \int_b^\eta \Sigma F_x dz + \bar{\rho}v_x(\eta)A - \bar{\rho}v_x(b)B. \qquad (43.26)$$

This equation can be manipulated into useful alternative forms by expanding the derivatives on the left-hand side to obtain

$$\begin{aligned}
&\bar{v}_x\bar{\rho}\left[\frac{\partial h}{\partial t} + \frac{\partial(h\bar{v}_x)}{\partial x} + \frac{\partial(h\bar{v}_y)}{\partial y} \right] + \bar{v}_x h\left[\frac{\partial \bar{\rho}}{\partial t} + \bar{v}_x\frac{\partial \bar{\rho}}{\partial x} + \bar{v}_y\frac{\partial \bar{\rho}}{\partial y} \right] \\
&+ \bar{\rho}h\left[\frac{\partial \bar{v}_x}{\partial t} + \bar{v}_x\frac{\partial \bar{v}_x}{\partial x} + \bar{v}_y\frac{\partial \bar{v}_x}{\partial y} \right] = \int_b^\eta \Sigma F_x dz + \bar{\rho}v_x(\eta)A - \bar{\rho}v_x(b)B. \qquad (43.27)
\end{aligned}$$

The second term in brackets in (43.27) can be replaced with the depth-averaged total time derivative $\bar{d}\bar{\rho}/\bar{d}t$, where $\bar{d}/\bar{d}t = \partial/\partial t + \bar{v}_x\partial/\partial x + \bar{v}_y\partial/\partial y$, and the first and third terms in brackets can be recombined to reduce (43.27) to

$$\begin{aligned}
&\bar{\rho}\left[\frac{\partial(h\bar{v}_x)}{\partial t} + \frac{\partial(h\bar{v}_x^2)}{\partial x} + \frac{\partial(h\bar{v}_x\bar{v}_y)}{\partial y} \right] + \bar{v}_x h\frac{\bar{d}\bar{\rho}}{\bar{d}t} \\
&= \int_b^\eta \Sigma F_x dz + \bar{\rho}v_x(\eta)A - \bar{\rho}v_x(b)B. \qquad (43.28)
\end{aligned}$$

This form of the x-momentum equation is called "conservative" because the left-hand side represents evolution of a conserved variable, x-momentum per unit area $dxdy$. The terms $\bar{\rho}v_x(\eta)A$ and $\bar{\rho}v_x(b)B$ on the right-hand side of (43.28) account for x-momentum carried into or out of the flow by material with $v_x \neq 0$ passing through its upper or lower boundaries.

An alternative, "primitive" form of the x-momentum equation is obtained by using (43.23) and $\bar{d}/\bar{d}t$ as defined earlier to replace the first term in brackets in (43.27) with $-(h/\bar{\rho})(\bar{d}\bar{\rho}/\bar{d}t) + A - B$, and then replace the second and third terms in brackets with $\bar{d}\bar{\rho}/\bar{d}t$ and $\bar{d}\bar{v}_x/\bar{d}t$, respectively. These substitutions result in cancelations that reduce (43.27) to

$$\bar{\rho}h\frac{\bar{d}\bar{v}_x}{\bar{d}t} = \int_b^\eta \Sigma F_x dz + \bar{\rho}v_x(\eta)A - \bar{\rho}v_x(b)B - \bar{\rho}\bar{v}_xA + \bar{\rho}\bar{v}_xB, \qquad (43.29)$$

Although (43.29) is correct mathematically, it describes evolution of $\bar{v}_x$, a variable that is not physically conserved. As a result, the right-hand side of (43.29) contains the added terms $-\bar{\rho}\bar{v}_xA$ and $+\bar{\rho}\bar{v}_xB$, which misleadingly appear to represent momentum sources or sinks not present in (43.26), (43.27), or (43.28). In fact, $-\bar{\rho}\bar{v}_xA$ and $+\bar{\rho}\bar{v}_xB$ merely account for terms cancelled from the left-hand side of (43.29), and this fact must be borne in mind if Lagrangian numerical methods that employ (43.29) are used to compute solutions.

Evaluation of the forcing term $\int_b^\eta \Sigma F_x\, dz$ on the right-hand sides of (43.24) and (43.26) through (43.29) employs Leibniz rule during depth integration of the stress-gradient components, which appear explicitly in (43.19). Three terms generated in this integration vanish because they involve $\tau_{xx}(\eta)$, $\tau_{yx}(\eta)$ or $\tau_{zx}(\eta)$,

which all equal zero owing to the stress-free condition of the upper flow boundary. The remaining terms yield

$$\int_b^\eta \Sigma F_x\, dz = \bar{\rho} g_x h - \int_b^\eta \left[\frac{\partial \tau_{xx}}{\partial x} + \frac{\partial \tau_{yx}}{\partial y} + \frac{\partial \tau_{zx}}{\partial z} \right] dz$$

$$= \bar{\rho} g h \sin\theta - \frac{\partial(\bar{\tau}_{xx} h)}{\partial x} - \tau_{xx}(b)\frac{\partial b}{\partial x} - \frac{\partial(\bar{\tau}_{yx} h)}{\partial y} - \tau_{yx}(b)\frac{\partial b}{\partial y} + \tau_{zx}(b). \tag{43.30}$$

Note that according to the sign convention used here, $\tau_{zx}(b) < 0$ when $\tau_{zx}(b)$ resists distortion associated with $[\partial v_x/\partial z]_{z=b} > 0$. Thus, in (43.30) and succeeding equations, the basal shear stress $\tau_{zx}(b)$ helps resist the gravitational driving term $\bar{\rho} g h \sin\theta$.

Simplification of (43.30) is possible if the bed surface remains parallel to the x–y plane during erosion or sedimentation, such that $\partial b/\partial x = 0$ and $\partial b/\partial y = 0$. Then (43.30) reduces to

$$\int_b^\eta \Sigma F_x\, dz = \bar{\rho} g h \sin\theta - \frac{\partial(\bar{\tau}_{xx} h)}{\partial x} - \frac{\partial(\bar{\tau}_{yx} h)}{\partial y} + \tau_{zx}(b). \tag{43.31}$$

Substitution of (43.31) in (43.28) enables the x-momentum equation to be written as

$$\bar{\rho}\left[\frac{\partial(h\bar{v}_x)}{\partial t} + \frac{\partial(h\bar{v}_x^2)}{\partial x} + \frac{\partial(h\bar{v}_x\bar{v}_y)}{\partial y} \right] + \bar{v}_x h \frac{\bar{d}\bar{\rho}}{\bar{d}t}$$

$$= \bar{\rho} g h \sin\theta - \frac{\partial(\bar{\tau}_{xx} h)}{\partial x} - \frac{\partial(\bar{\tau}_{yx} h)}{\partial y} + \tau_{zx}(b)$$

$$+ \bar{\rho} v_x(\eta) A - \bar{\rho} v_x(b) B, \tag{43.32}$$

and the y-component momentum equation has a form exactly analogous to that of (43.32). The z-component momentum equation is also closely analogous, but it is useful to write it explicitly because of its critical role in scaling and stress evaluation:

$$\bar{\rho}\left[\frac{\partial(h\bar{v}_z)}{\partial t} + \frac{\partial(h\bar{v}_z\bar{v}_x)}{\partial x} + \frac{\partial(h\bar{v}_z\bar{v}_y)}{\partial y} \right] + \bar{v}_z h \frac{\bar{d}\bar{\rho}}{\bar{d}t}$$

$$= -\bar{\rho} g h \cos\theta - \frac{\partial(\bar{\tau}_{xz} h)}{\partial x} - \frac{\partial(\bar{\tau}_{yz} h)}{\partial y}$$

$$+ \tau_{zz}(b) + \bar{\rho} v_z(\eta) A - \bar{\rho} v_z(b) B. \tag{43.33}$$

43.4.2 Scaling and the Shallow-Flow Approximation

Further simplification of the depth-integrated momentum-conservation equations relies on the identification of characteristic scales for all variables they contain. Scaling, in turn, leads to identification of small terms that can be neglected. As illustrated in Figure 43.4, the characteristic length of a debris flow can be defined as L, and the characteristic thickness can be defined as H, so that the length scale for the x and y coordinates is L and the length scale for the z coordinate is H. Similarly, the scale for b, η, and h (all measured in the z direction) is H. Because debris-flow motion is driven by gravitational potential, the scale for the velocity components in the x and y directions is $(gL)^{1/2}$, and the scale for the z-direction velocity component is $(gH)^{1/2}$. A z-direction velocity scale $\beta(gH)^{1/2}$, which is adjusted by the arbitrary factor β, applies to the erosion and sedimentation rates A and B, because the magnitudes of these quantities are poorly constrained. Values $\beta \ll 1$ seem probable in most circumstances, however. The time-scale for debris-flow motion $(L/g)^{1/2}$ is the downslope length scale L divided by the downslope velocity scale $(gL)^{1/2}$. The scale for $\bar{\rho}$ is an equilibrium value, such as the initial static value, $\bar{\rho}_0$. Finally, the scale for all stress components (τ_{xx}, τ_{yy}, τ_{zz}, τ_{yx}, τ_{zx}, τ_{yz}) is the equilibrium lithostatic stress, $\bar{\rho}_0 g H$. The use of these scales enables definition of the following dimensionless variables, denoted by asterisks:

$$x^* = x/L \quad y^* = y/L \quad z^* = z/H \quad t^* = t/(L/g)^{1/2}$$

$$v_x^* = v_x/(Lg)^{1/2} \quad v_y^* = v_y/(Lg)^{1/2} \quad v_z^* = v_z/(Hg)^{1/2}$$

$$h^* = h/H \quad \bar{\rho}^* = \bar{\rho}/\bar{\rho}_0$$

$$\eta^* = \eta/H \quad b^* = b/H \quad A^* = A/\beta(Hg)^{1/2} \quad B^* = B/\beta(Hg)^{1/2}$$

$$(\tau_{xx}^*, \tau_{yy}^*, \tau_{zz}^*, \tau_{yx}^*, \tau_{zx}^*, \tau_{yz}^*) = (\tau_{xx}, \tau_{yy}, \tau_{zz}, \tau_{yx}, \tau_{zx}, \tau_{yz})/\bar{\rho}_0 g H \tag{43.34}$$

Substitution of (43.34) into (43.32) and (43.33) results in scaled forms of the equations

$$\bar{\rho}^*\left[\frac{\partial(h^*\bar{v}_x^*)}{\partial t^*} + \frac{\partial(h^*\bar{v}_x^{*2})}{\partial x^*} + \frac{\partial(h\bar{v}_x^*\bar{v}_y^*)}{\partial y^*} \right] + \bar{v}_x^* h^* \frac{\bar{d}\bar{\rho}^*}{\bar{d}t^*}$$

$$= \bar{\rho}^* h^* \sin\theta - \varepsilon\left[\frac{\partial(\bar{\tau}_{xx}^* h^*)}{\partial x^*} + \frac{\partial(\bar{\tau}_{yx}^* h^*)}{\partial y^*} \right]$$

$$+ \tau_{zx}^*(b^*) + \varepsilon^{-1/2}\beta\bar{\rho}^*\left[v_x^*(\eta^*) A^* - v_x^*(b^*) B^* \right] \tag{43.35}$$

and

$$\varepsilon^{1/2}\bar{\rho}^*\left[\frac{\partial(h^*\bar{v}_z^*)}{\partial t^*} + \frac{\partial(h^*\bar{v}_z^*\bar{v}_x^*)}{\partial x^*} + \frac{\partial(h^*\bar{v}_z^*\bar{v}_y^*)}{\partial y^*} \right]$$

$$+ \varepsilon^{1/2}\bar{v}_z^* h^* \frac{\bar{d}\bar{\rho}^*}{\bar{d}t^*}$$

$$= -\bar{\rho}^* h^* \cos\theta - \varepsilon\left[\frac{\partial(\bar{\tau}_{xz}^* h^*)}{\partial x^*} + \frac{\partial(\bar{\tau}_{yz}^* h^*)}{\partial y^*} \right]$$

$$+ \tau_{zz}^*(b^*) + \beta\bar{\rho}^*\left[v_z^*(\eta^*) A^* - v_z^*(b^*) B^* \right], \tag{43.36}$$

where

$$\varepsilon = H/L \tag{43.37}$$

is a fundamental length-scale ratio. The condition $\varepsilon \ll 1$ commonly applies in debris flows, which generally have thicknesses much smaller than their lengths and widths. Neglect of all terms containing ε or $\varepsilon^{1/2}$ in (43.35) and (43.36) therefore constitutes a rigorous *shallow-flow approximation*. The factor ε does not appear in the mass-conservation Equation 43.23 when it is scaled using (43.34), implying that no terms in (43.23) can be neglected.

43.4.3 Stress Estimation

Several physical implications of the shallow-flow approximation are noteworthy. Most significantly, if $\beta \ll 1$ and the erosion and sedimentation terms involving A^* and B^* are neglected, the condition $\varepsilon \ll 1$ reduces (43.36) to a static balance between the basal normal stress and the slope-normal component of the debris weight,

$$\tau_{zz}^*(b^*) = \bar{\rho}^* h^* \cos\theta \quad \text{(or, dimensionally, } \tau_{zz}(b) = \bar{\rho} g h \cos\theta\text{)}. \tag{43.38}$$

This approximation is employed in most shallow-flow theories, and as shown in the following, it can be used as a basis for estimating the stress components in (43.35). If $\beta \neq 0$, however, (43.38) is modified by the flux of z-direction momentum due to debris entering or leaving the flow. If, for example, basal sedimentation occurs at a rate $B^* > 0$, accompanied by a downward basal velocity $v_z^*(b^*) < 0$, the term $\beta\bar{\rho}^* B^* v_z^*(b^*)$ reduces the basal normal stress $\tau_{zz}^*(b^*)$.

Estimation of the stress components in (43.32) or (43.35) hinges on the validity of (43.38) or some other approximation of the z-momentum balance, and on the use of a constitutive model such as the Coulomb equation (43.8). Substitution of (43.38) in (43.8), and inclusion of the viscous stresses specified in (43.7), enables the basal shear stress in (43.32) to be estimated as

$$\tau_{xz}(b) = -[\bar{\rho} g h \cos\theta - p_{bed}]\tan\phi(S) - 2\bar{n}\mu\left(\frac{\bar{v}_x}{h}\right), \tag{43.39}$$

where

- $\bar{\rho} g h \cos\theta$ $(=\sigma_{bed})$ is the total basal normal stress
- p_{bed} is the basal pore-fluid pressure
- $\bar{n}$ is the depth-averaged porosity
- $-2\bar{n}\mu(\bar{v}_x/h)$ is the pore-fluid stress associated with viscous shearing at an estimated depth-averaged rate $2\bar{v}_x/h$

Importantly, σ_{bed}, p_{bed}, h, and $\bar{v}_x$ are readily measured quantities, as illustrated in Figure 43.3.

Although the lateral stress-gradient terms $\partial(\bar{\tau}_{xx}h)/\partial x$ and $\partial(\bar{\tau}_{yx}h)/\partial y$ in (43.32) are typically small, as indicated by the factor ε that precedes them in (43.35), these terms are generally included in depth-averaged models because their neglect would leave only rigid-body forcing effects on the right-hand side of (43.32). The terms can be approximated by inferring that $\bar{\tau}_{zz} \approx \tau_{zz}(b)/2$ and $\bar{p} \approx p_{bed}/2$, and postulating that $\bar{\tau}_{xx} = \kappa_1\bar{\tau}_{zz} + \bar{p}$ and $\bar{\tau}_{yx} = \kappa_2\bar{\tau}_{zz} + \bar{n}\mu(\partial\bar{v}_x/\partial y)$, where κ_1 and κ_2 are proportionality coefficients (of order 1) that describe the magnitude of lateral stress transfer by solid grains, and $\bar{p}$ and $\bar{n}\mu(\partial\bar{v}_x/\partial y)$ are depth-averaged fluid stresses due to pressure and viscous shearing, respectively (Iverson and Denlinger 2001). The use of these expressions in conjunction with (43.38) yields

$$\frac{\partial(h\bar{\tau}_{xx})}{\partial x} = \frac{1}{2}\frac{\partial}{\partial x}\kappa_1[\bar{\rho} g h^2 \cos\theta - h p_{bed}] + \frac{1}{2}\frac{\partial(h p_{bed})}{\partial x} \tag{43.40}$$

$$\frac{\partial(h\bar{\tau}_{yx})}{\partial y} = \frac{1}{2}\frac{\partial}{\partial y}\kappa_2[\bar{\rho} g h^2 \cos\theta - h p_{bed}] + \bar{n}\mu\left[h\frac{\partial^2\bar{v}_x}{\partial y^2} + \frac{\partial h}{\partial y}\frac{\partial\bar{v}_x}{\partial y}\right] \tag{43.41}$$

Note that (43.40) reduces to the analogous expression used in conventional shallow-water theory, $\partial(h\bar{\tau}_{xx})/\partial x = \bar{\rho} g h \cos\theta(\partial h/\partial x)$, if $\bar{\rho}$ is constant and either $\kappa_1 = 1$ (implying hydrostatic intergranular stress), or $p_{bed} = \bar{\rho} g h \cos\theta$ (implying complete mixture liquefaction).

Equations 43.39 through 43.41 and analogous y-component equations provide mathematical closure of the depth-averaged conservation laws describing evolution of h, $\bar{v}_x$, and $\bar{v}_y$, but only if equations governing simultaneous evolution of p_{bed}, $\bar{n}$, and $\bar{\rho}$ are also specified—and only if erosion and sedimentation are negligible ($\beta \to 0$). Analyses of cases with $\beta \neq 0$ are in their earliest stages and are not presented here, but derivations of the depth-integrated evolution equations for p_{bed}, $\bar{n}$, and $\bar{\rho}$ are relatively straightforward.

43.4.4 Depth-Integrated Pore-Pressure Evolution

Depth integration of the pore-pressure evolution equation (43.17) relies on some simplifying approximations to obtain an equation that contains p_{bed} rather than p_e. Preliminary steps involve recasting (43.17) in terms of the total pore-fluid pressure, $p = p_e + \rho_f g(h - z)\cos\theta$, and invoking shallow-flow scaling that applies if $\varepsilon \ll 1$. This scaling indicates that $\partial^2 p/\partial z^2$ is much greater than $\partial^2 p/\partial x^2$ and $\partial^2 p/\partial y^2$ because $\partial^2/\partial z^2$ scales with $1/H^2$, whereas $\partial^2/\partial x^2$ and $\partial^2/\partial y^2$ scale with $1/L^2$. Consequent neglect of $\partial^2 p/\partial x^2$ and $\partial^2 p/\partial y^2$ reduces (43.17) to

$$\frac{dp}{dt} - \frac{k}{\alpha\mu}\frac{\partial^2 p}{\partial z^2} = \frac{d\sigma}{dt} - \frac{\dot{\gamma}\psi}{\alpha}. \tag{43.42}$$

Another step involves the use of the approximations $v_z = (z/h)\,dh/dt$, $v_x = \bar{v}_x$, and $v_y = \bar{v}_y$ to recast the total time derivatives in (43.42) as $d/dt = \bar{d}/\bar{d}t + (z/h)(\bar{d}h/\bar{d}t)\partial/\partial z$. Then (43.42) can be rewritten as

$$\frac{\bar{d}p}{\bar{d}t} - \frac{k}{\alpha\mu}\frac{\partial^2 p}{\partial z^2} = \frac{\bar{d}\sigma}{\bar{d}t} + \frac{z}{h}\frac{\bar{d}h}{\bar{d}t}\frac{\partial(\sigma - p)}{\partial z} - \frac{\dot{\gamma}\psi}{\alpha}. \tag{43.43}$$

Depth integration of (43.43) is accomplished term-by-term using Leibniz rule and applying the stress-free surface boundary conditions $p(\eta) = \sigma(\eta) = 0$, yielding

$$\frac{\bar{d}(\bar{p}h)}{\bar{d}t} - \frac{k}{\alpha\mu}\left[\left.\frac{\partial p}{\partial z}\right|_{z=\eta} + \rho_f g\cos\theta\right] = \frac{\bar{d}(\bar{\sigma}h)}{\bar{d}t} + (\bar{\sigma} - \bar{p})\frac{\bar{d}h}{\bar{d}t} - \sqrt{\bar{v}_x^2 + \bar{v}_y^2}\,\frac{\psi}{2\alpha}, \qquad (43.44)$$

where overbars denote depth-averaged variables and $\sqrt{\bar{v}_x^2 + \bar{v}_y^2}\,/2h$ is used to approximate the depth-averaged shear rate, $(1/h)\int_b^\eta \dot{\gamma}dz$. The term $\rho_f g\cos\theta$ arises in (43.44) from depth-integration of the pore-pressure diffusion term in (43.43) and application of a zero-flux basal boundary condition that requires the pore-pressure gradient at the bed to remain hydrostatic: $[\partial p/\partial z]_{z=b} = -\rho_f g\cos\theta$. The term $(\bar{\sigma} - \bar{p})\bar{d}h/\bar{d}t$ arises from depth-integrating the term that includes $\partial(\sigma - p)/\partial z$ in (43.43) by parts. This term cancels some other terms and thereby reduces (43.44) to

$$\frac{\bar{d}\bar{p}}{\bar{d}t} - \frac{k}{\alpha\mu h}\left[\left.\frac{\partial p}{\partial z}\right|_{z=\eta} + \rho_f g\cos\theta\right] = \frac{\bar{d}\bar{\sigma}}{\bar{d}t} - \sqrt{\bar{v}_x^2 + \bar{v}_y^2}\,\frac{\psi}{2h\alpha}, \qquad (43.45)$$

where

$$\bar{\sigma} = \frac{\bar{\tau}_{zz} + \bar{\tau}_{xx} + \bar{\tau}_{yy}}{3} = \frac{(1+2\kappa_1)}{6}\bar{\rho}gh\cos\theta \qquad (43.46)$$

and κ_1 is the lateral stress coefficient introduced in (43.40). Equation 43.45 retains two pore-pressure variables, p and $\bar{p}$, however, rather than the single desired variable, p_{bed}.

To express (43.45) in terms of p_{bed}, approximations of $\bar{p}$ and $[\partial p/\partial z]_{z=\eta}$ are necessary. First-order approximations assume that p varies linearly with depth, ranging from $p = p_{bed}$ at $z = b$ to $p = 0$ at $z = \eta$. This linear distribution of p implies that

$$\bar{p} = \frac{1}{2}p_{bed} \quad \left.\frac{\partial p}{\partial z}\right|_{z=\eta} = -\frac{p_{bed}}{h}. \qquad (43.47)$$

Higher-order (in z/h) approximations allow for nonlinearity of the pore-pressure profile, particularly near the bed (Savage and Iverson 2003), but such details complicate the results without revealing effects of fundamental importance, and they are omitted here for the sake of brevity. Substitution of (43.46) and (43.47) into (43.45) then yields

$$\frac{\bar{d}p_{bed}}{\bar{d}t} = \frac{-2k}{\alpha\mu h^2}\left[p_{bed} - \rho_f gh\cos\theta\right] + \frac{(1+2\kappa_1)g\cos\theta}{3}\left[\frac{\bar{d}(\bar{\rho}h)}{\bar{d}t}\right] - \sqrt{\bar{v}_x^2 + \bar{v}_y^2}\,\frac{\psi}{h\alpha}. \qquad (43.48)$$

The derivative $\bar{d}(\bar{\rho}h)/\bar{d}t$ can be eliminated from the right-hand side of (43.48) by using the mass-conservation equation (43.23) to find that $\bar{d}(\bar{\rho}h)/\bar{d}t = -\bar{\rho}[h(\partial\bar{v}_x/\partial x + \partial\bar{v}_y/\partial y) - A + B]$. Making this substitution in (43.48) yields the final form of the evolution equation for p_{bed}:

$$\frac{\bar{d}p_{bed}}{\bar{d}t} = \frac{-2k}{\alpha\mu h^2}\left[p_{bed} - \rho_f gh\cos\theta\right] - \bar{\rho}gh\cos\theta\frac{1+2\kappa_1}{3}\left[\frac{\partial\bar{v}_x}{\partial x} + \frac{\partial\bar{v}_y}{\partial y} - \frac{A-B}{h}\right] - \sqrt{\bar{v}_x^2 + \bar{v}_y^2}\,\frac{\psi}{h\alpha}. \qquad (43.49)$$

43.4.5 Depth-Integrated Porosity and Bulk Density Evolution

The derivation of the depth-integrated evolution equation for n utilizes the scaling inference $\partial^2 p/\partial z^2 \gg \partial^2 p/\partial x^2$ and $\partial^2 p/\partial z^2 \gg \partial^2 p/\partial y^2$ described above, and also utilizes the assumption $\rho = \bar{\rho}$, which implies that $n = \bar{n}$. Under these conditions, depth integration of Equation 43.15 yields

$$\frac{h}{1-\bar{n}}\frac{\bar{d}\bar{n}}{\bar{d}t} = \frac{k}{\mu}\left.\frac{\partial p_e}{\partial z}\right|_{z=b}^{z=\eta}. \qquad (43.50)$$

Like the preceding equations involving $\bar{d}/\bar{d}t$, this equation assumes that $v_x = \bar{v}_x$ and $v_y = \bar{v}_y$. The linear pore-pressure distribution defined in conjunction with (43.47) indicates that $\partial p_e/\partial z = -(p_{bed} - \rho_f gh\cos\theta)/h$, and use of this expression in (43.50) yields the evolution equation for $\bar{n}$:

$$\frac{\bar{d}\bar{n}}{\bar{d}t} = (1-\bar{n})\frac{-k}{h^2\mu}(p_{bed} - \rho_f gh\cos\theta). \qquad (43.51)$$

This result also provides an evolution equation for $\bar{\rho}$ if the debris remains saturated with pore fluid, because (43.3) implies that

$$\bar{\rho} = \rho_s(1-\bar{n}) + \rho_f\bar{n}. \qquad (43.52)$$

The similarity of terms on the right-hand side of (43.51) and some of those on the right-hand side of (43.49) is significant. Indeed, the unforced version of (43.49) can be substituted into (43.51) to reduce it to

$$\frac{1}{1-\bar{n}}\frac{\bar{d}\bar{n}}{\bar{d}t} = \frac{\alpha}{2}\frac{\bar{d}p_{bed}}{\bar{d}t} \qquad (43.53)$$

This equation implies that, in the absence of external forcing, $\bar{n}$ declines logarithmically as p_{bed} declines linearly. Such nonlinear behavior is typical of quasi-static, water-saturated granular debris as it consolidates during dissipation of pore-fluid pressure (Iverson 1997).

43.4.6 Model Summary

The system of depth-integrated equations governing simultaneous evolution of h, $h\overline{v}_x$, p_{bed}, $\overline{n}$, and $\overline{\rho}$ is (43.23), (43.32), (43.49), (43.51), and (43.52). In addition, (43.39) through (43.41) specify the stress terms that appear in (43.32). A system of equations exactly analogous to (43.32) and (43.39) through (43.41), but with x and y transposed, describes evolution of $h\overline{v}_y$. All stress calculations are predicated on (43.38), which approximates the z-momentum equation and constitutes the central postulate of the depth-integrated model.

43.5 Solution Techniques and Model Predictions

Numerical solution of the full set of model equations described above is the object of ongoing research. Two broad classes of techniques have proven useful for solving similar systems of conservation equations, such as the shallow-water equations and Savage-Hutter granular avalanche equations. One type of technique employs Lagrangian numerical methods in which the computational mesh translates with the local flow velocity. This approach has the advantage of replacing partial derivatives of the nonlinear terms on the left-hand side of (43.28) with total time derivatives such as that on the left-hand side of (43.29). Furthermore, these methods are relatively easy to implement if the flow path is simple (such as a uniformly inclined plane). Classical Lagrangian techniques have limited potential for computing motion across complex, 3D terrain, however, because deformation of the computational mesh can become exceedingly complicated. Meshless Lagrangian techniques such as those used in smooth-particle hydrodynamics may have promise, but their structure makes it difficult to determine if conservation equations are rigorously satisfied (McDougall and Hungr 2004).

A more rigorous approach utilizes a fixed, Eulerian computational mesh, but also requires the use of shock-capturing numerical methods to accurately account for the potentially severe effects of nonlinearities, which can give rise to discontinuous solutions. (Conventional finite-difference and finite-element methods tend to smear out these effects, leading to inaccurate solutions.) Finite-volume methods enable shock capturing by reframing the numerical problem as a series of elementary Riemann problems that describe fluxes of conserved variables between adjacent computational cells (e.g., Denlinger and Iverson 2001, 2004; Pitman and Le 2005). Such methods also lend themselves to adaptive mesh refinement (AMR), a sophisticated technique that can greatly accelerate computation speeds by automatically implementing mesh refinement only where high resolution is needed (George and LeVeque 2008).

Despite significant advances, application of computational models to forecasting behavior of debris flows and rock avalanches remains in its earliest stages, largely because most model predictions have not been subject to rigorous, controlled tests. Instead, models have generally been calibrated to fit field observations (mostly by tuning resistive stress terms), and such models cannot be regarded as truly predictive. A basis for more stringent model testing is provided by recently acquired experimental data such as those summarized in Figure 43.3. The availability of such data, along with increasingly sophisticated numerical methods, makes prospects for better understanding and modeling of debris flows appear promising.

References

Bear, J. 1972. *Dynamics of Fluids in Porous Media.* New York: Dover.

Costa, J.E. and G.P. Williams. 1984. Debris-flow dynamics (videotape). U.S. Geological Survey Open-file Report 84-606. Videotape.

Denlinger, R.P. and R.M. Iverson. 2001. Flow of variably fluidized granular masses across three-dimensional terrain: 2. Numerical predictions and experimental tests. *Journal Geophysical Research* 106: 553–566.

Denlinger, R.P. and R.M. Iverson. 2004. Granular avalanches across irregular three-dimensional terrain: 1. Theory and computation. *Journal Geophysical Research* 109: F01014, doi:10.1029/2003JF000085.

Desai, C.S. and H.J. Siriwardane. 1984. *Constitutive Laws for Engineering Materials, with Emphasis on Geological Materials.* Englewood Cliffs, NJ: Prentice-Hall.

Forterre, Y. and O. Pouliquen. 2008. Flows of dense granular media. *Annual Review of Fluid Mechanics* 40: 1–24.

George, D.L. and R.J. LeVeque. 2008. High-resolution methods and adaptive refinement for tsunami propagation and inundation. In *Hyperbolic Problems: Theory, Numerics, Application.* eds. S. Benzoni-Gavage and D. Serre, pp. 541–549. Berlin, Germany: Springer.

Gidaspow, D. 1994. *Multiphase Flow and Fluidization.* Boston, MA: Academic Press.

Gray, J.M.N.T. and B.P. Kokelaar. 2010. Large particle segregation, transport and accumulation in granular free-surface flows. *Journal Fluid Mechanics* 652: 105–137.

Hunt, M.L., R. Zenit, C.S. Campbell, and C.E. Brennen. 2002. Revisiting the 1954 suspension experiments of R.A. Bagnold. *Journal Fluid Mechanics* 452: 1–24.

Iverson, R.M. 1997. The physics of debris flows. *Reviews of Geophysics* 35: 245–296.

Iverson, R.M. 2009. Elements of an improved model of debris-flow motion. In *Powders and Grains 2009*, ed. M. Nakagawa and S. Luding, pp. 9–16. Melville, NY: American Institute of Physics.

Iverson, R.M. and R.P. Denlinger. 2001. Flow of variably fluidized granular masses across three-dimensional terrain: 1. Coulomb mixture theory. *Journal Geophysical Research* 106: 537–552.

Iverson, R.M., M. Logan, R.G. LaHusen, and M. Berti. 2010. The perfect debris flow: Aggregated results from 28 large-scale experiments. *Journal Geophysical Research* 115: doi:10.1029/2009JF001514.

Kowalski, J. 2008. Two-phase modeling of debris flows. Dr. Sci. dissertation, Zurich, Switzerland: ETH Zurich.

Logan, M. and R.M. Iverson. 2007. Video documentation of experiments at the USGS debris-flow flume, 1992–2006. U.S. Geological Survey Open-file Report 2007-1315. http://pubs.usgs.gov/of/2007/1315/

McDougall, S. and O. Hungr. 2004. A model for the analysis of rapid landslide motion across three-dimensional terrain. *Canadian Geotechnical Journal* 41: 1084–1097.

Pailha, M. and O. Pouliquen. 2009. A two-phase flow description of the initiation of underwater granular avalanches. *Journal of Fluid Mechanics* 633: 115–135.

Pitman, E.B. and L. Le. 2005. A two-fluid model for avalanche and debris flow. *Philosophical Transactions Royal Society London* 363: 1573–1601.

Savage, S.B. and R.M. Iverson. 2003. Surge dynamics coupled to pore-pressure evolution in debris flows. In *Debris-Flow Hazards Mitigation: Mechanics, Prediction, and Assessment*, ed. D. Rickenmann and C.-L. Chen, Vol. 1, pp. 503–514. Rotterdam, the Netherlands: Millpress.

Sharp, R.P. and L.H. Nobles. 1953. Mudflow of 1941 at Wrightwood, southern California. *Geological Society America Bulletin* 64: 547–560.

Sidle, R.C. and M. Chigira. 2004. Landslides and debris flows strike Kyushu, Japan. *EOS* 85: 145–156.

Takahashi, T. 2007. *Debris Flow Mechanics, Prediction and Countermeasures*. London, U.K.: Taylor & Francis.